



# Mechanical characterization and numerical modeling of laser-sintered TPE lattice structures

Christina Kummert<sup>1,3,a)</sup>, Hans-Joachim Schmid<sup>1,3</sup> , Lena Risse<sup>2,3</sup>, Gunter Kullmer<sup>2,3</sup>

<sup>1</sup> Particle Technology Group, Pohlweg 47-49, 33098 Paderborn, Germany

<sup>2</sup> Institute of Applied Mechanics, Paderborn University, Pohlweg 47-49, 33098 Paderborn, Germany

<sup>3</sup> Direct Manufacturing Research Center, Paderborn University, Mersinweg 3, 33100 Paderborn, Germany

<sup>a)</sup> Address all correspondence to this author. e-mail: christina.kummert@dmrc.de

Received: 6 May 2021; accepted: 27 July 2021; published online: 17 August 2021

**Additive Manufacturing provides the opportunity to produce tailored and complex structures economically. The use of lattice structures in combination with a thermoplastic elastomer enables the generation of structures with configurable properties by varying the cell parameters. Since there is only little knowledge about the producibility of lattice structures made of TPE in the laser sintering process and the resulting mechanical properties, different kinds of lattice structures are investigated within this work. The cell type, cell size and strut thickness of these structures are varied and analyzed. Within the experimental characterization of Dodecahedron-cell static and cyclic compression tests of sandwich structures are focused. The material exhibits hyperelastic and plastic properties and also the Mullins-Effect. For the later design of real TPE structures, the use of numerical methods helps to reduce time and costs. The preceding experimental investigations are used to develop a concept for the numerical modeling of TPE lattice structures.**

## Introduction

Selective Laser Sintering (SLS) is a powder bed based process in which the energy input of the laser on a powder layer leads to localized melting and fusing of polymer particles. In the next step, this layer is lowered to apply a new layer of powder and exposed again with the laser to create a layer bond. A plastic component is thus successively created, with the surrounding powder serving as support material, which is subsequently removed. This process offers high productivity due to the usability of three-dimensional space and the possibility to create complex geometries such as grid structures [1]. As a restriction, the removal of the remaining powder has to be mentioned at this point, which is generally a problem with closed cavities but also with too small free volumes such as gaps [2]. Furthermore, only a few materials have been sufficiently investigated for the SLS process for a later application.

The material used in this work is the thermoplastic elastomer (TPE-A) PrimePart ST from EOS, a polyether blockamide (PEBA) for the laser sintering process (SLS). It has an elongation at break of 200% and is therefore particularly suitable for applications where high formability is required [3]. Beside the high degree of flexibility, the material shows good resistance to

chemicals and temperature over a wide range from  $-40\text{ }^{\circ}\text{C}$  to  $90\text{ }^{\circ}\text{C}$  [4]. These properties make the material versatile in use.

However, the availability of material data as well as information on the production-oriented design of components made of this material is not yet as comprehensive as for the standard SLS material polyamide 12. In particular, lattice structures in combination with elastically deformable materials offer the possibility of realizing configurable and later on graded mechanical properties by varying the design of the lattice cells and can be manufactured with almost no design restrictions in the laser sintering process. However, there are also restrictions and process parameters such as scaling that must be adapted and especially the wall thickness and build orientation influence the resulting mechanical properties [5].

But first of all, the manufacturability of the lattices is limited due to the filigree structures which might be damaged already in the post process. Further, especially elastomeric powders show comparatively low flowability [6, 7] which may lead to poor removability of the powder from the gaps in the post process [2].

The fabrication of lattice structures is an interesting possibility to use the advantages of additive manufacturing processes. Complex structures in which material is only used where it is

necessary offers a good compromise between lightweight design and mechanical performance.

Lattice structures are used in a variety of technical applications or for design reasons. By using additive manufacturing processes, components with grids can be produced from a variety of unit cells without great effort. Each unit cell has specific mechanical properties depending on its structure (cell type, cell size, strut thickness, etc.) [8, 9]. If these are used systematically, it is possible to develop structures with individual, stress-adapted grading. Other studies also used the benefits of additive manufacturing for the fabrication of lattice structures. In the field of polymers, the design for the SLA [10, 11] and the FDM [12, 13] process and subsequent compression behavior in particular have been widely investigated.

Laser-sintered lattice structures have also been investigated in other works, but these were different materials. In addition to the polyamide 12 mentioned above [13–18], studies on various lattice structures made of laser-sintered TPU have been published [14, 16, 19]. The mechanical properties of the different lattice structures depend particularly on the geometry and cell density [13, 18, 20]. Furthermore, the experimental data are used for FE analyses [10, 13, 20] to model the material behavior

as a lattice structure. However, investigations about using the laser sintering PEBA a polyamide based thermoplastic elastomer to generate lattice structures are scarce [1] but expands the range of materials additionally to the TPUs available so far [4].

In order to be able to use the described advantages of grid structures made of TPE with individual grading of the mechanical properties, this paper first investigates the manufacturability of various types of lattice structures and then their mechanical behavior under static and cyclical pressure loading. First, different cell types are examined and afterwards the focus is on the dodecahedron cell type. For a later component design, the experimentally gained knowledge is transferred into a material model for the numerical modeling of such lattice structures.

## Results

### Manufacturability of lattice structures using laser sintering

Table 1 shows the results of the preliminary investigations about the manufacturability of lattice structures in tabular form. In general, when unpacking and free blasting (compressed air and glass beads) of the lattice structures, it can be seen that regardless

**TABLE 1:** Manufacturability of lattice structures.

Cell type	Strut thickness / mm	Cell size / mm			
		2.5	5	10	15
Dode	0.6	-	-	-	-
	1	✗	✗	✓	✓
	1.5	✗	✗	✗	✓
	2	✗	✗	✗	✓
Cube	0.6	-	-	-	-
	1	✗	✓	-	-
	1.5	✗	✓	✓	✓
	2	✗	✓	✓	✓
FCCZ	0.6	-	-	-	-
	1	✗	✓	✓	-
	1.5	✗	✗	✓	✓
	2	✗	✗	✓	✓
Star	0.6	-	-	-	-
	1	✗	✗	✓	✓
	1.5	✗	✗	✗	✓
	2	✗	✗	✗	✗
		✓ feasible	- failure		
		✗ Powder not completely removable	✗ enclosed volumes		

of the strut diameter a cell size of 2.5 mm cannot be produced, since actually free volumes remain sealed. Furthermore, the cell size of 5 mm is also not feasible for the Dode and Star cells. Therefore, these cell types require a minimum cell size of more than 5 mm. The density of these cells can be taken into account as a reason for this. Both structures have a high number of struts per unit cell, resulting in a higher density compared to the cube or FCCZ cell. The cell size must therefore be large relative to the strut thickness and the number of struts to form an optimal cell structure. In Table 2 the calculated specific cell density, where the material volume of the struts is related to the total volume of the cell, is shown exemplarily for some Dode cell sizes and strut thicknesses. It can be seen that the density increases with increasing strut thickness and lower cell size. Comparing with the results of the manufacturability in Table 1, for a specific cell density of 0.9 and smaller, powder can be removed completely.

It can also be stated that a strut thickness of 0.6 mm always leads to a failure of the structure already in the post-process. Therefore, a minimum size of 10 mm is required for the Dode and Star cell and a minimum strut thickness of 1.0 mm is recommended. The cube and FCCZ cells, on the other hand, can be successfully manufactured even with a cell size of 5 mm. The minimum strut thickness of 1.0 mm is also recommended. For the FCCZ and cube cell it is still recommended to use a minimum strut diameter of more than 1.0 mm for cell sizes of 10 mm and above.

For the mechanical characterization of TPE lattice structures compression test specimens are used as core composites according to DIN 53291 [21], whereby the lattices are realized between two cover layers (50 × 50 mm<sup>2</sup>), as shown in Fig. 7c. These sandwich structures are also initially examined for their manufacturability, but due to the previous investigations on 2 × 2 × 2 composites, only strut thickness of 1 mm and 1.5 mm are considered here for cell sizes of 5 mm (not for the Dode and Star cell), 10 mm and 15 mm.

For the Dode and Star cell, the same statements can be made for the investigated parameters as for the 2 × 2 × 2 composites. However, in the case of the cube cell premature failure occurs in the core composites with 1.5 mm strut thickness and 15 mm cell size. In the case of the FCCZ cell, the powder can still not be completely removed if the core composite is made of 5 mm

cells. The cover layers seem to make powder removal more difficult here.

In general, it can be seen when unpacking and free blasting the lattice structures, regardless of the strut diameter and cell type, a cell size of 2.5 mm cannot be manufactured, since actually free volumes remain closed. Furthermore, the cell size of 5 mm is also not feasible for 2 × 2 × 2 structure, so that for sandwich structures only bigger cell sizes are tested and required. This might be due to the density of the cell structure. The cell size must be large enough relative to the strut thickness and the number of struts in order to form a perfect cell structure.

It can also be stated that a strut thickness of 0.6 mm always leads to a failure of the structure already in the post-process. All in all, a minimum size of 10 mm is required and a minimum strut thickness of 1.0 mm is recommended.

### Mechanical characterization

The evaluation of the quasi-static test results shows (see Fig. 1a) that the qualitative progression in the stress–strain diagram is similar for all samples. After an initially linear phase up to about 0.1 mm/mm tensile elongation, a further increase in tensile stress takes place, which flattens more and more with increasing elongation. The maximum tensile stress is reached when failure occurs. It can be seen that the TPE under investigation qualitatively moves between the behavior of a thermoplastic and an elastomer. To examine this in more detail, a load increase test is carried out below.

The stress–strain diagram of the load cycle test in Fig. 1b) shows very clearly that each time the load is relieved, the material has a lower stress. According to this, the TPE, analogous to the Mullins effect, also shows a softening of the material. However, in contrast to elastomers, the material is also plastically deformed. This suggests that the thermoplastic segments are irreversibly deformed and thus permanently deform the overall composite. Furthermore, hysteresis effects can be observed. Overall, the TPE again exhibits the characteristics of a thermoplastic and an elastomer. With regard to plastic deformation, it can be seen that this increases linearly as a function of the applied elongation.

The diagram in Fig. 5b shows the results of the compressive strength for different strut thicknesses and cell sizes of sandwich structures. It can be seen, that the compressive strength increases with increasing strut thickness. Furthermore, a comparison of the cell sizes shows that at 10 mm, the strength is much higher than in cells of 15 mm. The analysis of the compression test specimens during testing (see Fig. 6) shows that the structure deforms in the nodes like pseudo-joints. Further, the struts exhibit plastic deformation after the test procedure which is discussed more in detail in “Discussion” section. It can therefore be assumed that the mechanical properties change during

**TABLE 2:** Specific cell density of some Dodecahedron structures.

Cell size/mm		
Strut thickness/mm	10	15
0.6	0.03	0.01
1.0	0.09	0.04
1.5	0.20	0.09
2	0.34	0.15

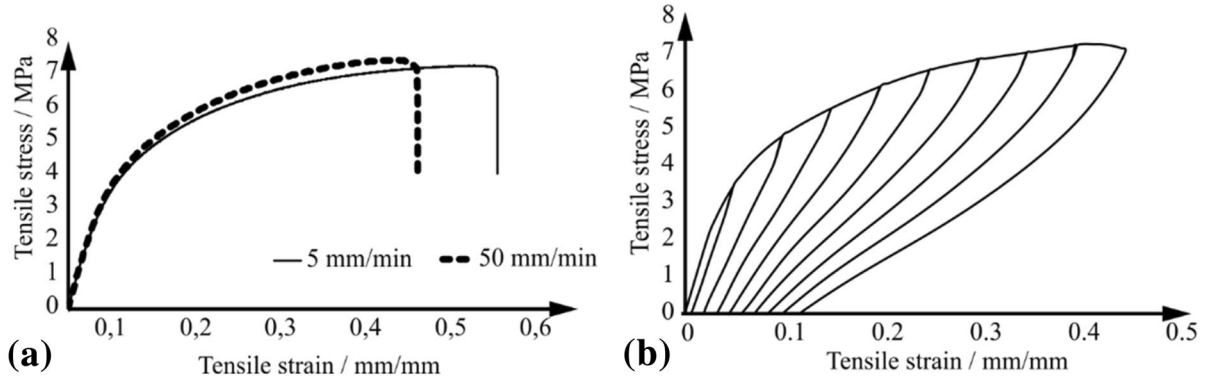


**Figure 1:** (a) Stress–strain behavior of TPE tensile specimen (type 1, ISO 37 [10], full material) at different test speeds and (b) Stress–strain behavior in the load increase test (tensile test type 1, ISO 37).

a repetitive test procedure. In Fig. 2 the results of the repetitive compression test are shown. Overall, it can be observed that the same pattern is obtained in each test: The struts fold together as compression increases. There is no failure and no visible damage to the struts.

During the tests it could be observed, that the compressive strength of all specimens visibly decreases after the first test run and converges towards a limit value with a further number of test repetitions. The deformation mechanism during the test run provides an explanation for this behavior. Elastic and plastic deformation of the struts takes place during compression. The elastic component deforms back to its original position after the compression force has been released. On the other hand, the plastic deformation permanently deforms the composite, which leads to a weakening of the structure. This leads to an overall significant reduction in compressive strength.

To illustrate this, Fig. 2 shows all 20 test runs of the cell size of 15 mm and strut thickness of 1.5 mm in the stress–strain diagram. For the first test run, a gradual increase can be observed, which approximates a linear course with a larger number of test repetitions. At the first loading, the pseudo-joints at the nodes were not yet deformed (possibly even plastically deformed). Due to the deformation, the pseudo-joints lose stiffness, so that afterwards the deformation can take place more easily and almost without steps. The range in which a high degree of energy is absorbed by the compression of the cell structure increasingly disappears.

### Numerical modelling of cell structures

Based on the literature references, the one-time quasi-static load and also a cyclic load on the shoulder tension bar is modelled with both the elasto-plastic Johnson Cook plasticity model and the

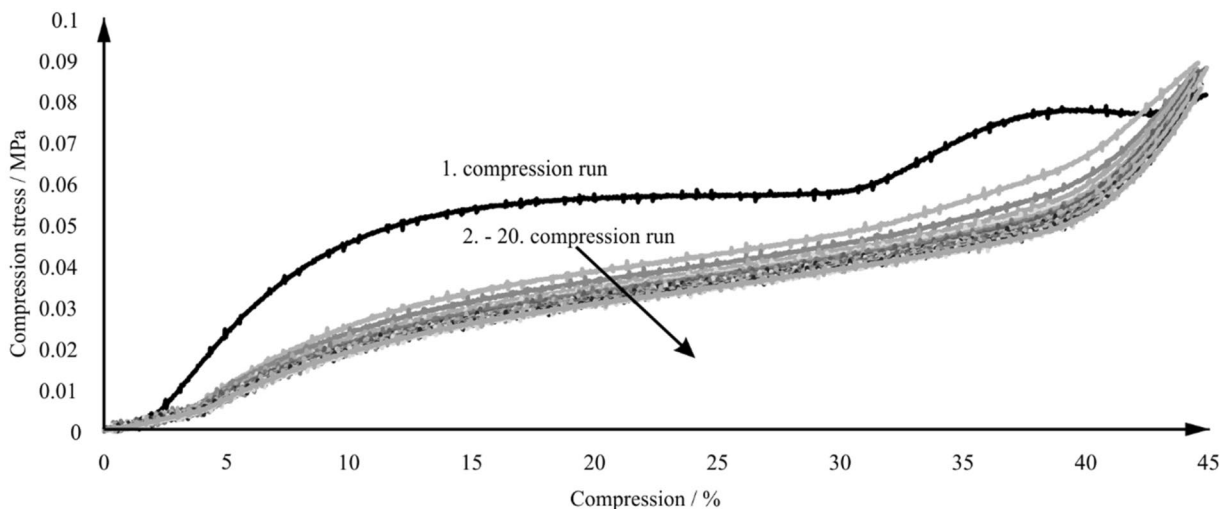


**Figure 2:** Compressive-stress curves of 20 test runs (15 mm cell size and 1.5 mm strut thickness).

hyper-elastic Marlow model. The original curve is well represented by both approaches, but both models have significant weaknesses, so that realistic cyclical modeling requires optimization of the numerical material model. When using the Johnson Cook model, the plasticity of the material is overestimated. The Marlow model, on the other hand, shows no difference to the original curve when re-loaded, as no plasticity is taken into account.

In order to generate a possibility of cyclic simulation of TPE structures, a new model is being developed that combines the assumptions of the models documented in literature. The development of the combined material model is illustrated in Fig. 3.

In the experimental investigations (Fig. 3a), the investigated TPE exhibits a mixture of hyperelastic, plastic and viscoelastic behavior. Furthermore, hysteresis effects and the Mullins effect are to be detected under cyclic loading. The developed material model is initially only valid for short-term loads. Visco-elastic effects are negligible for this assumption but can be implemented later without great effort. The hysteresis effects are also neglected, as Abaqus does not support this. The experimental data from the load increase test are used to provide the material map of hyper-elasticity, plasticity and the Mullins effect with the required parameters. For hyperelasticity (Fig. 3b), the original curve smoothed by a regression function is assumed to be the Marlow approach.

A widely used approach offers the formulation of the stress-strain curve as a function of the strain energy density  $W$ . For a linear-elastic curve, the following relationship applies as an example [22]:

$$W = \frac{1}{2} \sigma_{ij} \varepsilon_{ij} \quad (1)$$

Since rubber elasticity is non-linear, the equation above cannot be applied. For this reason, the general form must be used to determine the strain energy density [23]:

$$W = \sum_{i,j=1}^3 \int_0^{\varepsilon_{ij}} \sigma_{ij} d\varepsilon_{ij} \quad (2)$$

One way to solve the summation of this integral is to fit the experimental results. A well-known approach to this is the Marlow model, where the stress-strain curve is directly integrated from the uniaxial material test [23]:

$$W = \int_0^{\varepsilon_{ij}-1} \sigma(\varepsilon)_{ij} d\varepsilon_{ij} \quad (3)$$

The advantage of this model is that the stress-strain behavior can be represented exactly for the uniaxial loading case. The entire course is assumed to be hyperelastic, so that no plastic and viscous effects are included. Another significant advantage is the low experimental effort. To model the hyperelasticity with the Marlow approach, only the stress-strain characteristics of an uniaxial material test are required. At the same time, sufficient stability of the hyperelasticity is generated over the entire strain range, since the complete deformation range is included in the hyperelastic approach.

For plasticity (Fig. 3c), a nonlinear flow curve is required. By means of this flow curve, the plastic deformation ratio at a certain stress is to be defined. The isotropic plasticity is used as material map for this purpose. The plastic strain is given in

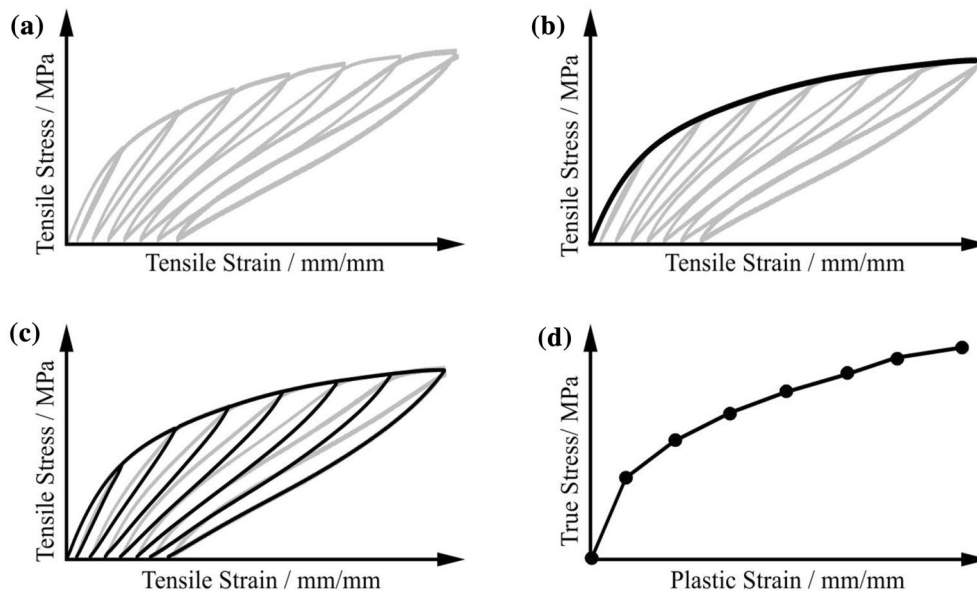


**Figure 3:** Basics for the development of the combined material model (a) Experimental data from the load increase test (b) Modeling of hyperelasticity (c) Modelling of the Mullins effect (d) modelling of isotropic plasticity.

tabular form as a function of the true stress. The characteristic values are determined from the stress–strain diagram of the load increase test, in which the technical stress of the respective plastic strain is plotted. In order to use the data in the material card, it must be converted into the true stress on the basis of internal software specifications. Since the definition of plasticity at an initial yield stress of 0 MPa leads to numerical problems, a value of 0.1 MPa is used as the initial stress. From this true stress onwards, the material begins to flow plastically. Within the context of the new model, the Mullins effect as a form of a damage function is also to be implemented in the hyperelastic function of the deformation energy density.

To describe the Mullins effect, the Ogden–Roxburgh model is implemented into the hyperelastic model. The basic idea behind this is to extend the description of the strain energy density via a variable  $\eta$  and damage function ( $\zeta$ ) [21]. The variable  $\zeta$  defines the degree of damage and consequently lowers the strain energy density [23].

$$\begin{aligned}
 W &= \zeta W_{Dev} + \phi(\zeta) + W_{Vol} \\
 \text{with } \zeta &= 1 - \frac{1}{r} \operatorname{erf}\left(\frac{W_{Dev}^m - W_{Dev}}{m + \beta W_{Dev}^m}\right) \\
 \phi(\zeta) &= \int_1^\zeta \zeta d\zeta + (1 - \zeta) W_{Dev}^m
 \end{aligned}
 \tag{4}$$

With  $\zeta$ : damage variable;  $\phi(\zeta)$ : damage function;  $W_{Dev}^m$ : All-time maximum of strain energy density;  $r, m, \beta$ : Material properties.

It can be seen from Formula 4 that only the deviatoric component of the strain energy density is used. The reason for this is that incompressible behavior is again assumed and the volumetric component is omitted accordingly.

The expression of the Mullins effect is mainly controlled by the damage variable  $\eta$ , which takes values between 0 and 1. The exact value is determined by various parameters within an error

function. The parameters  $r, m$  and  $\beta$  describe the discharge process [24].  $W_{Dev}^m$  represents the all-time maximum of the strain density, which defines the range of material softening [23].

Since the exact calculation of the parameters is very complex on the basis of the mathematical relationships, numerical methods should also be used here to determine the model parameters. Abaqus makes it possible to determine the characteristic values by entering experimental data. The material tests required for this are again uniaxial and, if necessary, additional biaxial and planar tensile or compression tests. It is important that several load cycles with loading and unloading phases are recorded when carrying out the test. The amount of loading can be adjusted depending on the application [25].

In Abaqus, the stress–strain curves of the load and unloading curves can be entered in tabular form. To avoid numerical problems, the curves are approximated by a regression (Fig. 3d).

In order to check the applicability of the developed model, the experimental results of the load increase test are compared with the numerical simulation using the newly developed combined material model in Fig. 4a. The consideration of the Mullins effect and the irreversible deformation results in an overall good approximation to the experimental data. The model was derived and validated for one strain rate only. Since no significant strain rate influence could be determined in the experimental tests before, an applicability in a larger strain rate range can be concluded.

In the following, the transferability of the developed simulation model to the cyclically compressively loaded lattice structures is examined and, if necessary, adjustments are made. First, it becomes clear that even small deviations in the strut thickness of the lattice structure have a large influence on the results. For the later application of the material model in the design of real structures, a high dimensional accuracy in the subsequent construction process must therefore be guaranteed. In the subsequent numerical simulation of the load increase test (Fig. 4b)

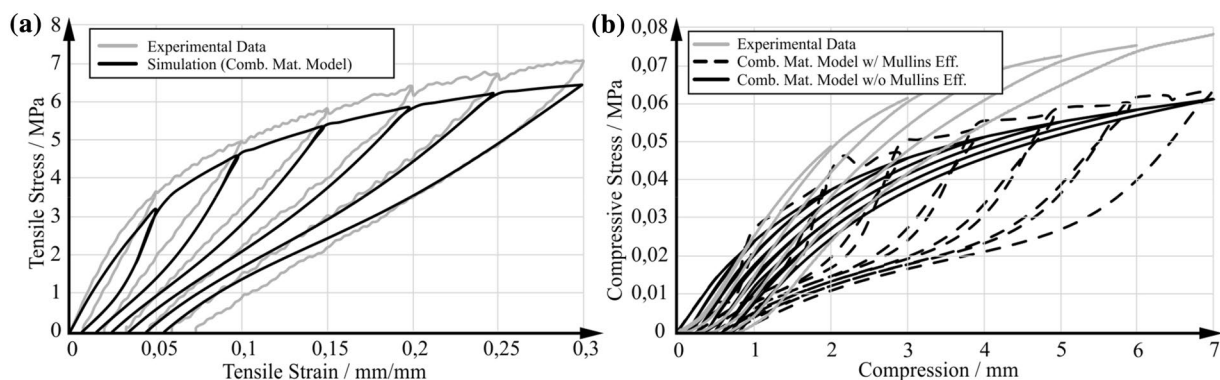


**Figure 4:** Comparison of the experimental data of the load increase test with the numerical material models (a) Validation of the combined material model on the shoulder tension rod (b) Influence of the Mullins effect using the example of the 20.5 mm Dode-cell with 2.0 mm strut thickness.

it becomes clear that the combined material model developed overestimates the material softening of the grid structure due to the Mullins effect. In the experimental investigations, this almost does not occur, so that the material map of the Mullins effect should be removed for cyclic simulations. The better agreement of the stress-strain curves with the fitted model is also shown in Fig. 4b.

### Discussion

During the experimental investigation of compression test on the lattice structures it could be stated that no failure of the struts appears, but a slight plastic deformation was visible after the compression tests. A lattice structure can be considered as a special framework in which the nodes act as pseudo-joints. The dode cell has a densely packed structure with 32 struts and 22 nodes per unit. The spatial counting criterion is therefore calculated as follows [26]:

$$f = 32 - 3 \cdot 22 + 6 = -28 < 0 \quad (5)$$

A value below 0 means that the system is statically indeterminate. Accordingly, the cell deforms in the joints but the struts themselves are not bent. Figure 5a shows the results of the compression tests on 15 mm cells for different strut thicknesses in the stress-strain diagram as well as the different deformation states.

Up to a compression of approx. 15% to 20%, a stronger increase in compressive stress is recorded, which then leads to the plateau stress (20% to 28%). First, the joints of the diamond-shaped struts in the center of the lattice structure deform. The increase is due to the existing bending stiffness of the pseudo-joint, which must first be overcome. When the plateau is reached, the struts are folded until they lie on block. Afterwards, a further increase in compressive stress up to approx. 35% to 45% compression is observed, since the bending stiffness

of the outer joints opposes further compression and must be overcome. During the following stress plateau, the outer struts collapse completely and lie compressed on top of each other. During further compression the transition to the compacting area takes place. From this compression onwards, a strong increase in compressive stress can be observed, which is used as a criterion for aborting the test. It can generally be seen that with increasing strut thickness, the compressive stress increases. For strut thicknesses of 1.2 mm and 1.5 mm, a local stress minimum must be detected at high compression. This could be attributed to the struts turning over during the compression process. At a strut thickness of 1.7 mm this behavior no longer occurs due to the higher stability.

The maximum compressive stress before the compacting area is defined as compressive strength which is here the local stress maximum at a compression of approx. 35 to 45%. It was also used to determine the compressive strength in Fig. 5b.

For the numerical modelling it was detected that the models for grid structures have to be adjusted because the Mullins effect could not be detected in the experimental results. Possibly the absence of the Mullins effect is due to the locally limited higher stress on the grid structure. The basic tendency that a higher stiffness of the cell structure can be detected by the experimental investigations compared to the numerical model can be attributed to powder adhesion in the area of the joints of the struts with each other. In this way, the joints are stiffened and the deformation of the cell is made more difficult. This accumulation of material is not taken into account in the cells which are modelled as geometrically ideal. To further compare the numerical behavior with the experimental results, the resulting deformation of the cell structure is analyzed. Identical to the experiment, the highest deformation in the simulation is also caused by buckling of the central struts. The struts in contact with the respective cover layers do not show any visible

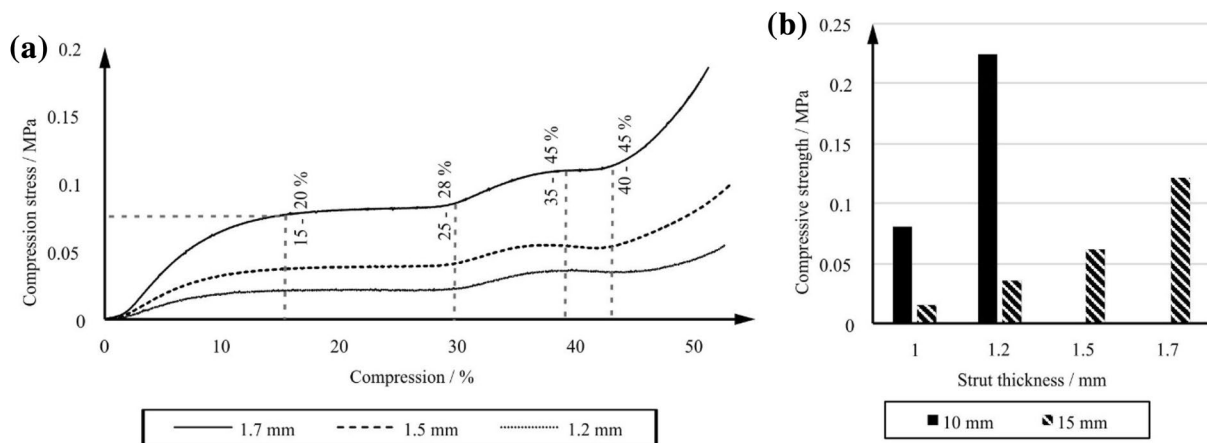


**Figure 5:** Compression test of sandwich structure (a) Stress-compression curve of 15 mm cell size (b) Compressive strength of 10 mm and 15 mm cell.

deformation. A comparison of the experimentally determined with the numerically resulting deformation behavior is shown in Fig. 6.

It is clear that there is very good agreement, so that the model is basically valid and deviations can only be justified by idealization of the geometry compared to the real component. If these deviations are relevant for later applications, adjustments can be made.

## Conclusion and outlook

In the context of this work, the producibility of different lattice structures made of TPE in the laser sintering process was investigated. It was determined that this is limited by a high density, i.e. a high number and thickness of struts per cell, as powder removability is no longer possible. A further restriction is the minimum strut thickness of 1 mm, since smaller strut diameters lead to premature failure already in the post-process.

Before the grid structures were mechanically characterized, the material was examined in static and cyclic tensile tests. This showed that the material has properties of thermoplastics and elastomers and shows the Mullins effect in the load increase test. The compression test on core composites with dodecahedron cells also shows that a reduction in the core layer height and an increase in the strut thickness increase the compressive strength. It is therefore possible to set different or graded properties by varying the cell geometry. Furthermore, the grid structure shows a stepwise increase of the compressive stress, which is due to the successive yielding of the joints. During the repeated compression test of the grid structure, this behavior is only apparent in the first test run. The irreversible deformation causes the cells to remain increasingly compressed. The Mullins effect is also no longer observed here.

With the knowledge of the mechanical behavior from the experimental investigations, a numerical material model could be developed which includes the material behavior under quasi-static and cyclic loading. The idea is based on the combination of different material maps, where each of them

represents a characteristic property of the material. This can be used in the future for the design of first real structures. Further, the approach of this work from design to manufacturability, mechanical characterization and numerical modeling of laser sintering lattice structures can be applied for other laser sintering materials.

## Material and methods

### Design of lattice structures for laser sintering

The investigated material TPE is used with a refresh rate of 50/50 on the laser sintering system EOSINT P395. Further, a layer thickness of 150  $\mu\text{m}$  and the parameter set “Thinwall” are used to fabricate the lattice structures at 137  $^{\circ}\text{C}$  process temperature.

The software 3-MATIC from the manufacturer MATERIALISE is used to create the lattice structures to be investigated. The software offers both a unit cell database and the possibility to generate user-defined cell types. The unit cells can then be arranged periodically in a predefined volume after the cell properties (type, size, strut thickness) have been defined. The cell types studied are the cube, FCCZ, dodecahedron (dode) and star cell (see Fig. 7). In order to evaluate the manufacturability, the removability of unsintered powder, enclosed volumes as well as the failure of the lattice structure in the post-process are considered in preliminary investigations. This is initially done using cube-shaped composed structure from  $2 \times 2 \times 2$  unit cells, as shown in Fig. 7a) as an example. Furthermore, the cell size (2.5 mm, 5 mm, 10 mm and 15 mm) as well as the strut thickness (0.6 mm, 1.0 mm, 1.5 mm and 2.0 mm), which always represents the diameter of the circular struts, are varied. The selection of dimensions is based on former investigations in connection with laser sintered PA12 lattice structures [27] and these studied parameters can also be taken systematically from the Table 1. Each test specimen is manufactured three times distributed over the build space in order to exclude a build position dependency of the resulting properties which is known for laser sintering [28].

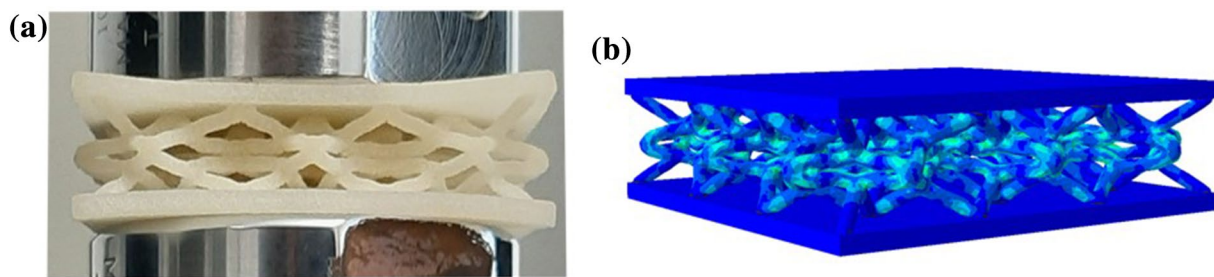


**Figure 6:** Comparison of the deformation behavior (a) Experimentally determined deformation of the lattice structure (b) Deformation behavior of the numerically modeled lattice structure.



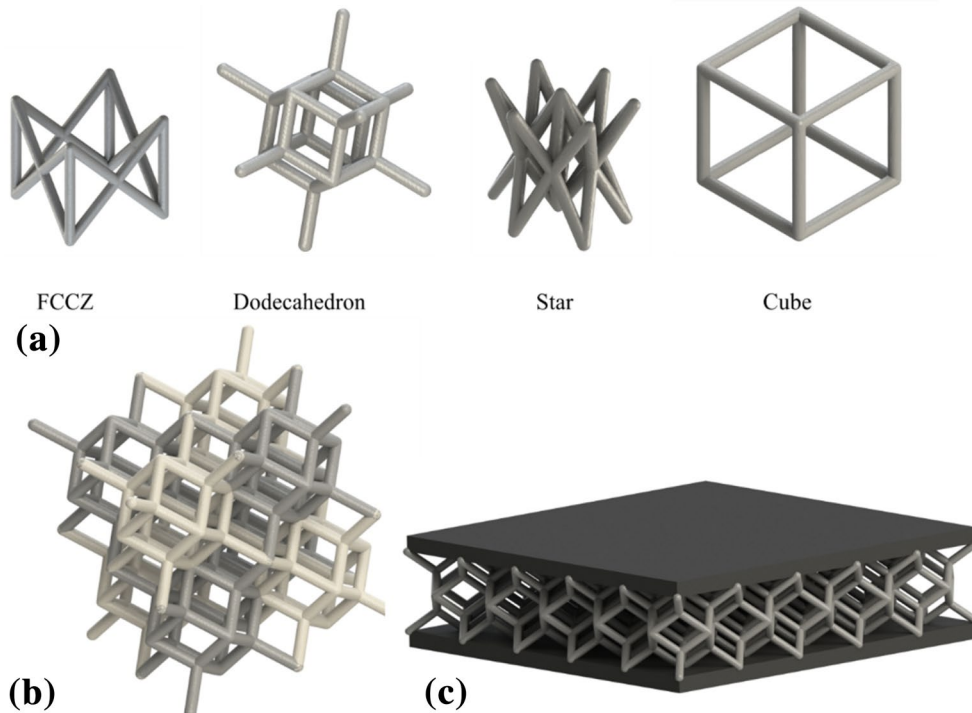


**Figure 7:** (a) Cell types under investigation. (b) Dodecahedron  $2 \times 2 \times 2$  structure. (c) sandwich structure according to DIN 53291 [21].

### Mechanical characterization

In the present work, quasi-static and fatigue properties of the tensile bar are investigated for mechanical characterization and static and cyclic pressure tests of sandwich lattice structures are carried out, which are used as a basis for the later numerical modeling. Altogether, it is of particular interest how the lattice structure behaves under mechanical load.

Since the struts of the grid structures also experience tensile stress during compression, a material test is carried out first in a tensile test. A bending load is also applied but is subdivided again into tensile and compressive stress in the strut cross-section and therefore not considered further. For tensile tests the type 1 shoulder bar according to ISO 37 is used as the specimen. The tests are performed on a universal testing machine 5569 from the manufacturer Instron. Further, the tensile force is recorded by a 5 kN load cell at a test speed of 5 mm/min or 50 mm/min, to regard the influence of the test speed. Three specimens are used for each test speed.

Elastomers experience material softening under cyclic loading. In theory, this so-called Mullins effect [29] represents an ideally elastic phenomenon. However, thermoplastics do not show this effect. Instead, they exhibit plastic strain that lead to irreversible deformations. In order to be able to assess these phenomena in the case of TPE, a cyclic test is performed on the Zwick HC10 dynamic tensile testing machine from Zwick/Roell in accordance with ISO 37. The specimen is loaded at a constant test speed of 50 mm/min with a defined

strain amplitude. The amplitude increases with each cycle by a distance of 2.5 mm, while in parallel the force is recorded with a 10 kN load cell.

The compression test on lattice structures is based on the standard DIN 53291 [21] for testing core composites (see Fig. 7c)) To reduce the large scale of the presented experimental design, in the following investigations, the lattice structure in the core layer is concentrated on the dodecahedron cell, since the focus here is on cells with sufficient cell elasticity, energy absorption and ductility. In the future, also the dependence of the mechanical properties on the cell type can be considered in more detail, in which case the cell density should be kept constant.

Here again, different cell sizes (10 and 15 mm) and strut thicknesses are regarded, but strut thicknesses are adapted after the results of the manufacturability tests to 1, 1.2, 1.5 and 1.7 mm. As two different cell sizes are tested, different compression areas must be considered. Specimen cover areas of  $50 \times 50 \text{ mm}^2$  are suitable and filled with  $5 \times 5$  10 mm cells. For 15 mm cells  $3 \times 3$  structures fill specimen areas of  $45 \times 45 \text{ mm}^2$ .

However, to evaluate compression results equally compression forces are referred to the area of the cover layer of the particular lattice structure. This allows a correction to be made when determining the compressive stress. In addition, the compression  $\varepsilon$  in the stress-compression diagram is not given as an absolute value, but as a percentage. It is calculated from the compressed path relative to the total height of the unloaded specimen:

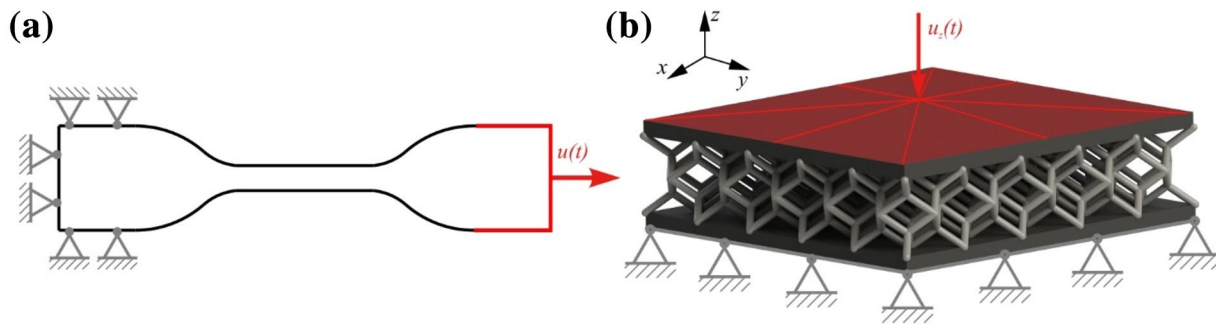


**Figure 8:** Boundary conditions for the numerical simulations (a) shoulder tension rod (b) sandwich-structure.

$$\varepsilon = \frac{\text{compressed path in mm}}{\text{total specimen height in mm}} \times 100 \quad (6)$$

The static compression tests are done on the universal testing machine Instron 5569 again with a speed of 5 mm/min and 50 kN load cell. During these tests two parallel plates compress the specimen and stop as soon as failure occurs or the struts of the lattice structure lie compressed on each other (see Fig. 6a). Further, repetitive compression tests are conducted. For this purpose, specimens with a cell size of 15 mm and a strut thickness 1.5 mm are tested. Each specimen is subjected to 20 consecutive compression tests. The test parameters and conditions are the same as in the previous compression tests (DIN 53291 [21]). The structure is compressed and released again until the beginning of the compacting range.

### Numerical modelling of cell structures

In order to provide a basis for the subsequent efficient design of components with lattice structures made of TPE, the experimental results are used to define a concept for the numerical modeling of these TPE cell structures. In the literature only few modeling approaches are documented that are investigated first regarding their usability.

According to Tobajas et al., the classical hyperelastic material models examined by them show good agreement in their short-term behavior [29]. Nevertheless, there are other material characteristics which are more or less pronounced depending on the TPE class investigated. In [18], reference is also made to the varying degrees of strain-rate dependence of TPEs, so that under certain circumstances viscoelasticity should also be taken into account in the material model. In [19] a combination of a hyperelastic approach and a plasticity model is recommended and developed. Basically, it becomes clear that the numerical representation of the material behavior of thermoplastic elastomers, especially the behavior of more complex geometries or grid structures has been little or not documented and investigated so far. Using the material models from literature, it becomes obvious that only static

load cases can be reproduced correctly in the numerical simulations. Based on those findings from the literature, an advanced concept for numerical modelling of cyclic loading situations of TPE lattice structures is developed.

The numerical simulations are performed using the software ABAQUS. The software is used for the numerical calculation of static and dynamic mechanical problems. ABAQUS is used for the model design, the calculation and the subsequent post-processing. The concept development starts using a shoulder tension rod and afterwards a sandwich structure. The FE-models are built up according to the experimental boundary conditions (see Fig. 8). In case of the shoulder tension rod (Fig. 8a) one side is clamped firmly while the other side is loaded with a defined displacement. The specimen is subjected to a path-controlled amplitude that includes a continuous increase in displacement in each cycle.

The examined lattice structures are inserted between two pressure plates defined as rigid bodies and firmly connected (Fig. 8b). The lower plate is firmly clamped, while the upper plate is subjected to a defined movement, which compresses the bond cyclically. Since preliminary investigations showed that a simplified assumption of the struts as beam elements does not lead to realistic results, the grid structures are meshed with 3D volume elements. The meshing is done with C3D10MH elements; the lattice structure is connected to the top surfaces via a “tie-contact”. The selected element type provided the most stable simulation results.

### Funding

Open Access funding enabled and organized by Projekt DEAL. Not applicable.

### Declarations

**Conflict of interest** The authors declare that they have no known competing financial interests or personal relationships that could have appeared to influence the work reported in this paper.

## Open Access

This article is licensed under a Creative Commons Attribution 4.0 International License, which permits use, sharing, adaptation, distribution and reproduction in any medium or format, as long as you give appropriate credit to the original author(s) and the source, provide a link to the Creative Commons licence, and indicate if changes were made. The images or other third party material in this article are included in the article's Creative Commons licence, unless indicated otherwise in a credit line to the material. If material is not included in the article's Creative Commons licence and your intended use is not permitted by statutory regulation or exceeds the permitted use, you will need to obtain permission directly from the copyright holder. To view a copy of this licence, visit <http://creativecommons.org/licenses/by/4.0/>.

## References

1. M. Schmid, *Selektives Lasersintern (SLS) Mit Kunststoffen* (Technologie, Prozesse und Werkstoffe Hanser Verlag, München, 2015)
2. L.W. Hunter, D. Brackett, N. Brierley, J. Yang, M.M. Attallah, Assessment of trapped powder removal and inspection strategies for powder bed fusion techniques. *Int J Adv Manuf Technol* **106**(9–10), 4521–4532 (2020). <https://doi.org/10.1007/s00170-020-04930-w>
3. EOS (2020): Materialdatenblatt PrimePart ST PEBA 2301. <https://www.eos.info/de/additive-fertigung/3d-druck-kunststoffe/polymer-material-werkstoffe/tpe>. Accessed 18 Aug 2020
4. M. Holmes, Additive manufacturing continues composites market growth. *Reinf. Plast.* **63**(6), 296–301 (2019). <https://doi.org/10.1016/j.repl.2018.12.070>
5. S.L. Sindinger, C. Kralovec, D. Tasch, M. Schagerl, Thickness dependent anisotropy of mechanical properties and inhomogeneous porosity characteristics in laser-sintered polyamide 12 specimens. *Addit. Manuf.* **33**(4), 101141 (2020). <https://doi.org/10.1016/j.addma.2020.101141>
6. M. Van den Eynde, L. Verbelen, P. Van Puyvelde, Assessing polymer powder flow for the application of laser sintering. *Powder Technol.* **286**, 151–155 (2015). <https://doi.org/10.1016/j.powtec.2015.08.004>
7. S. Ziegelmeier, F. Wöllecke, C.J. Tuck, R.D. Goodridge, R.J. Hague, Aging behavior of thermoplastic elastomers in the laser sintering process. *J. Mater. Res.* **29**(17), 1841–1851 (2014). <https://doi.org/10.1557/jmr.2014.172>
8. S.J. Merkt, Qualifizierung von generativ gefertigten Gitterstrukturen für maßgeschneiderte Bauteilfunktionen. Dissertation, RWTH Aachen, 2015
9. R. Prithvirajan, C. Balakumar, G. Arumaikkannu, Effect of strut diameter on compressive behaviour of selective laser sintered polyamide rhombic dodecahedron lattice. *Mater. Today* **31**(5), 361 (2020). <https://doi.org/10.1016/j.matpr.2020.09.684>
10. M. Keshavarzan, M. Kadkhodaei, F. Forooghi, An investigation into compressive responses of shape memory polymeric cellular lattice structures fabricated by vat polymerization additive manufacturing. *Polym. Test.* **91**(2018), 106832 (2020). <https://doi.org/10.1016/j.polymertesting.2020.106832>
11. S. Wang, J. Wang, Y. Xu, W. Zhang, J. Zhu, Compressive behavior and energy absorption of polymeric lattice structures made by additive manufacturing. *Front. Mech. Eng.* **15**(2), 319–327 (2020). <https://doi.org/10.1007/s11465-019-0549-7>
12. M. Al Rifaie, A. Mian, R. Srinivasan, Compression behavior of three-dimensional printed polymer lattice structures. *Proc. IMechE* **233**(8), 1574–1584 (2019). <https://doi.org/10.1177/1464420718770475>
13. M. El Jai, N. Saidou, H. Bachiri, Mathematical design and preliminary mechanical analysis of the new lattice structure: “GE-SEZ\*” structure processed by ABS polymer and FDM technology. *Prog Addit Manuf* **6**(1), 93–118 (2021). <https://doi.org/10.1007/s40964-020-00148-0>
14. I. Maskery, L. Sturm, A.O. Aremu, A. Panesar, C.B. Williams, C.J. Tuck, R.D. Wildman, I.A. Ashcroft, R.J.M. Hague, Insights into the mechanical properties of several triply periodic minimal surface lattice structures made by polymer additive manufacturing. *Polymer* **152**(62), 71 (2018). <https://doi.org/10.1016/j.polymer.2017.11.049>
15. D. Menge, S. Josupeit, P. Delfs, H.-J. Schmid, Herstellbarkeit und mechanische Charakterisierung von lasergesinterten Gitterstrukturen. in: *Additive Fertigung von Bauteilen und Strukturen*. (Springer Fachmedien, Wiesbaden, 2017), pp. 105–120
16. N. Clayton, Mechanical Properties of Laser-Sintered-Nylon Diamond Lattices. Dissertation University of South Florida, 2015
17. L. Bai, C. Gong, X. Chen, Y. Sun, L. Xin, H. Pu, Y. Peng, J. Luo, Mechanical properties and energy absorption capabilities of functionally graded lattice structures: experiments and simulations. *Int. J. Mech. Sci.* **182**, 105735 (2020). <https://doi.org/10.1016/j.ijmecsci.2020.105735>
18. X. Jin, G.X. Li, M. Zhang, Optimal design of three-dimensional non-uniform nylon lattice structures for selective laser sintering manufacturing. *Adv. Mech. Eng.* **10**(7), 168781401879083 (2018). <https://doi.org/10.1177/1687814018790833>
19. F. Shen, S. Yuan, Y. Guo, B. Zhao, J. Bai, M. Qwamizadeh, C.K. Chua, J. Wei, K. Zhou, Energy Absorption of thermoplastic polyurethane lattice structures via 3D printing: modeling and prediction. *Int. J. Appl. Mech.* **08**, 07 (2016). <https://doi.org/10.1142/S1758825116400068>
20. A. Kumar, L. Collini, A. Daurel, J.Y. Jeng, Design and additive manufacturing of closed cells from supportless lattice structure. *Addit. Manuf.* **33**(2–3), 101168 (2020). <https://doi.org/10.1016/j.addma.2020.101168>

21. DIN 53291. Prüfung von Kernverbunden. Druckversuch senkrecht zur Deckschichtebene, Standard Beuth (1973)
22. R. Tobajas, E. Ibaraz, L. Gracia, A comparative study of hyperelastic constitutive models to characterize the behaviour of a polymer used in automotive engines, University of Zaragoza, Conference Paper, 2nd International Electronic Conference on Materials, 2016
23. R. Tobajas, D. Elduque, E. Ibaraz, C. Javierre, A.F. Canteli, L. Gracia, Visco-Hyperelastic model with damage for simulating cyclic thermoplastic elastomers behavior applied to an industrial component. *Artikel aus Polymers* **10**(6), 668 (2018)
24. T. Scherer, Verhalten und Grenze der Beanspruchbarkeit elastischer Klebverbindungen, Dissertation, Fachbereich Maschinenbau und Verfahrenstechnik der Technischen Universität Kaiserslautern, 2014
25. R.W. Ogden, D.G. Roxburgh, *A Pseudo-Elastic Model for the Mullins Effect in Filled Rubber*, *Artikel Aus Der The Royal Society* *04/2016, Seiten 2861 Bis 2877* (University Gardens, Department of Mathematics, 2016)
26. C. Petersen, *Stahlbau* (Springer Fachmedien, Wiesbaden, 2013)
27. S. Josupeit, P. Delfs, D. Menge, H.J. Schmid, Manufacturability and mechanical characterization of laser sintered lattice structures. *Solid Freeform Fabr.* (2016)
28. C. Kummert, S. Josupeit, H.-J. Schmid, Thermoplastic elastomer part color as function of temperature histories and oxygen atmosphere during selective laser sintering. *JOM* **70**(3), 425–430 (2018). <https://doi.org/10.1007/s11837-017-2658-2>
29. Tobajas, R.; Ibaraz, E.; Gracia, L. A comparative study of hyperelastic constitutive models to characterize the behaviour of a polymer used in automotive engines. Conference Paper, University of Zaragoza, 2nd International Electronic Conference on Materials. <https://doi.org/10.3390/ecm-2-A002> (2016)